Efficient manifolds tracing for planar maps

David Ciro, Iberê L. Caldas, Ricardo L. Viana, and Todd E. Evans

Citation: Chaos **28**, 093106 (2018); doi: 10.1063/1.5027698
View online: https://doi.org/10.1063/1.5027698
View Table of Contents: http://aip.scitation.org/toc/cha/28/9
Published by the American Institute of Physics

Efficient manifolds tracing for planar maps

David Ciro,[1,a)] Iberê L. Caldas,[2] Ricardo L. Viana,[1] and Todd E. Evans[3]
[1]*Department of Physics, Federal University of Paraná, Curitiba, Paraná 81531-990, Brazil*
[2]*Department of Applied Physics, University of São Paulo, São Paulo, São Paulo 05508-090, Brazil*
[3]*General Atomics, P.O. Box 85608, San Diego, California 92186-5608, USA*

(Received 5 March 2018; accepted 16 July 2018; published online 11 September 2018)

In this work, we introduce an exact calculation method and an approximation technique for tracing the invariant manifolds of unstable periodic orbits of planar maps. The exact method relies on an adaptive refinement procedure that prevents redundant calculations occurring in other approaches, and the approximated method relies on a novel interpolation approach based on normal displacement functions. The resulting approximated manifold is precise when compared to the exact one, and its relative computational cost falls like the inverse of the manifold length. To present the tracing method, we obtain the invariant manifolds of the Chirikov-Taylor map, and as an application we illustrate the transition from homoclinic to heteroclinic chaos in the Duffing oscillator that leads from localized chaos to global chaotic motion. *Published by AIP Publishing.* https://doi.org/10.1063/1.5027698

Invariant manifolds are the underlying structure that delimit chaotic regions in the phase space and determine the transport channels induced by periodic orbits in the sea of chaos. The calculation of these invariants is important for the characterization of chaotic transport in diverse areas of interest, like magnetically confined plasmas and turbulent flows, and play an important role in the description of transport barriers. The methods introduced in this work are ideal for mappings involving intensive calculations like numerical function inversion or the numerical integration of ordinary differential equations between crossings through a surface of section. Our approximation method is based on an intuitive geometrical decomposition of the manifolds in bare and fine details and allows us to determine a suitable discretization for the curve without requiring numerical optimization.

I. INTRODUCTION

In dynamical systems, the determination of unstable periodic orbits and their invariant manifolds is a problem on its own and is fundamental to understanding the underlying structure of the chaotic orbits of planar maps.[1] These manifolds provide the skeleton for chaotic dynamics and are relevant in physical applications for the interpretation of the transport induced by non-integrability.[2,3]

Physically, invariant manifolds determine the geometrical features of advection and delimit the extension of irregular flows. For instance, in magnetically confined plasmas, a small non-axisymmetric magnetic field induces Hamiltonian chaos near the plasma edge of single-null tokamak discharges.[4–8] In this situation, the invariant manifolds of the magnetic saddle can be related to the heat flux patterns where the confinement chamber interacts with the plasma.[9,10] In analogous systems, time-dependent perturbations lead to orbit transfers between otherwise isolated regions of bistable non-linear oscillators.[11] Here, invariant manifolds determine the transport channels between the phase space domains.

From the dynamics point of view, manifold tracing is required for determining the geometry of the basins of attraction of chaotic sets,[12] and can be used to identify homoclinic and heteroclinic intersections which are contained in non-attracting invariant sets that play a fundamental role on the description of the dynamics of typical chaotic orbits in the phase space.[13] Although global quantities like the Lyapunov exponents allow us to determine numerically the bifurcation parameters, they do not, in general, provide details on the type of bifurcation that takes place. In this situation, precise invariant manifolds tracing determines clearly the topological mechanisms that take place during the bifurcations and accounts for physically relevant features, like regions of enhanced transport or the destruction of transport barriers.[14]

In some situations, the geometry of the manifolds can be estimated through the mapping of a large collection of orbits close to the saddle, a procedure similar to the one used to determine chaotic saddles.[15–18] However, without an ordering scheme and refinement, this method is computationally expensive and limited in resolution.

In this work, we introduce an *exact* and an approximation method to calculate the invariant manifolds of periodic saddles of planar maps. The maps in question can be explicit or induced by three-dimensional flows. Both calculations are based on the manifold decomposition in primary segments introduced by Hobson.[19] The *exact* method relies on the efficient calculation of primary segments from a single seed segment near the saddle, while the approximated method is based on the determination of reliable interpolants for arbitrary primary segments. The latter is specially relevant for maps induced by flows, where lengthy numerical integrations are required to produce a single iteration of the Poincaré map. This allows us to deal with the increase in length of the manifold segments due to the stretching and folding mechanism inherent to the chaotic dynamics.

[a)]Also at: Department of Applied Physics, University of São Paulo, São Paulo, SP 05508-090, Brazil; electronic mail: davidcirotaborda@usp.br

The approximation method involving the primary segments interpolation has been discussed before by Hobson[19] and Krauskopf,[20] and more detailed implementations were made by Goodman and Wróbel[21] and references therein. In this work, we introduce a versatile interpolation approach based on the curve decomposition in bare and fine details, which allow us to focus on different aspects of the manifold separately. The bare details of the curve are determined by a discretization procedure that determines an appropriate set of nodes containing most of the curve information, while the fine details are contained in a normal displacement function or *shape function* which ensures the smoothness of the manifold. The presented normal displacement description is new to our knowledge and can be easily implemented, containing a single set of adjustable parameters which can be fixed from intuitive geometrical conditions, complementing other approaches based on Catmull-Rom splines.[21] The resulting approximation method gives the invariant manifold as a continuous parametric curve from which we can measure the distance to the discretized manifold obtained from the exact calculation. This allows us to estimate the approximation error that, in general, is well below an estimated baseline. The approximation procedure is numerically stable and more efficient than the exact one, making it ideal for fast and precise calculations.

The methods presented in this work are specific for one-dimensional manifolds of planar maps. Other sophisticated methods are available for tracing manifolds for continuous dynamical systems,[22] which can then be used to intersect the surface of section instead of using a Poincaré map. Also, parametrization methods[23,24] are available for obtaining a patched manifold in discrete systems with arbitrary precision. In contrast to these methods, our simpler approach can be easily implemented by a non-specialist and is robust enough to deal with fairly complex manifolds. This work is intended to enable the reader to trace exact and approximated manifolds with a reliable numerical procedure, without dipping into the subject of numerical interpolation or parametrization functions.

The paper is organized as follows: in Sec. II, we present a review on invariant manifolds and their decomposition in primary segments. In Sec. III, we introduce an approximation method to obtain the zeroth segment of the manifold to machine precision. In Sec. V, we present an *exact* calculation method and in Sec. VI, we introduce its approximated version, where the interpolation procedure is detailed. In Sec. VII, we show an example application of the manifold tracing for bi-stable systems where the transition from homoclinic to heteroclinic chaos is used to explain the transition from alternating chaos to global chaos. In Sec. VIII, we present our conclusions and perspectives.

II. INVARIANT MANIFOLDS AND PRIMARY SEGMENTS

In this review section, we want to introduce the concept of invariant manifolds for planar maps and show their decomposition in primary segments. We also show, formally, the method to obtain any primary segment from a single known segment which will be discussed in the following section.

Without loss of generality, we will develop our discussion around the Poincaré maps of three-dimensional flows, since they represent a situation in which we do not have access to a closed-form expression for the planar map of interest. Consider the dynamical system

$$\frac{dx}{dt} = f(x), \tag{1}$$

where $x \in \mathbb{R}^3$ and $f : \mathbb{R}^3 \to \mathbb{R}^3$. The solution $\phi^t(x_0)$ of this differential equation takes an initial condition $x_0 \in \mathbb{R}^3$ and maps it to a new point $x \in \mathbb{R}^3$ for a given $t \in \mathbb{R}$. Now, consider an orientable two-dimensional surface Σ which is transverse to the flow everywhere, so that orbits starting in Σ must eventually return to Σ. Then, the Poincaré map T is a diffeomorphism $T : \Sigma \to \Sigma$ such that $y = T(x)$, where $x, y \in \Sigma$ and $y = \phi^\tau(x)$ for the smallest $\tau > 0$ such that the flow traverses Σ always in the same direction (Fig. 1). Analogously, the *inverse map* T^{-1} is such that $x = T^{-1}(y)$, where $x = \phi^\tau(y)$ for the largest $\tau < 0$.

A fixed point $x^* \in \Sigma$ satisfies $T(x^*) = x^*$, which means that the orbit starting in x^* is closed or periodic. For the case of interest, x^* is a saddle point, i.e., the Jacobian matrix of T has real eigenvalues $\{\lambda_s, \lambda_u\}$, such that $|\lambda_s| < 1$ and $|\lambda_u| > 1$.

The unstable manifold of x^*, $\mathcal{W}_u(x^*)$, is the collection of points that converge to x^* under T^{-1}, and the stable one $\mathcal{W}_s(x^*)$ is the collection that converge to x^* under T. Formally, we can write[13]

$$\mathcal{W}_u(x^*) = \{x \in \Sigma : T^{-n}(x) \to x^*, \text{as } n \to \infty\}, \tag{2}$$

$$\mathcal{W}_s(x^*) = \{x \in \Sigma : T^{n}(x) \to x^*, \text{as } n \to \infty\}. \tag{3}$$

For the numerical calculation of the invariant manifolds, it is useful to develop an ordering scheme that allows us to calculate them recursively, for this we resort to the concept of *primary segments*.[19] A primary segment based on x is a continuous subset of the manifold $P_{s,u}(x) \subset \mathcal{W}_{s,u}(x^*)$, containing every point in $\mathcal{W}_{s,u}(x^*)$ between x and $T(x)$, including x but not $T(x)$. Notice that, if $y \in P_u(x)$, then $T(y) \notin P_u(x)$, but clearly $T(y) \in P_u[T(x)]$, i.e., every point inside $P_u(x)$ has an image in the next primary segment and a pre-image in the previous one, and this is also valid for the base point x (Fig. 2). Without loss of generality, we will continue this discussion in terms of the unstable manifold, since the definitions and methods are analogous for the stable one.

The unstable manifold can be written as the union of all primary segments based on the images of an arbitrary

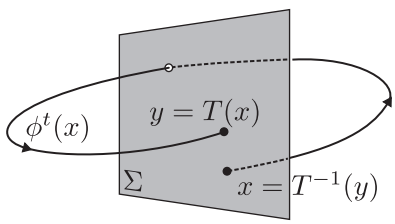

FIG. 1. Poincaré map as the first return to the surface Σ in a specified direction.

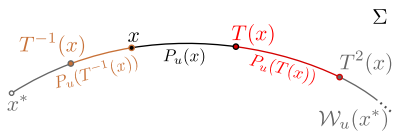

FIG. 2. The unstable manifold can be subdivided as a sequence of primary segments based on the images and pre-images of an arbitrary point of the manifold.

$x \in \mathcal{W}_u(x^*)$,

$$\mathcal{W}_u(x^*) = \bigcup_{n=-\infty}^{\infty} P_u[T^n(x)]. \tag{4}$$

Since every point in $P_u(x)$ has an image in $P_u[T(x)]$, we can say that the primary segment based on $T(x)$ is given by

$$P_u[T(x)] = T[P_u(x)], \tag{5}$$

where $T[A]$ is the set obtained after mapping every element of A. This implies that the manifold can be obtained by joining subsequent mappings of an arbitrary primary segment

$$\mathcal{W}_u(x^*) = \bigcup_{n=-\infty}^{\infty} T^n[P_u(x)]. \tag{6}$$

Consequently, if we know every point in any primary segment, we can map them forward and backward repeatedly to obtain the desired extent of the manifold. This is the theoretical basis of interpolation methods,[19,21] and it is valid for both conservative and dissipative diffeomorphisms.

III. APPROXIMATING THE ZEROTH SEGMENT

Now, we need to determine at least one primary segment of the manifold. This can be done to any desired precision in the region near the saddle point and, here, we illustrate this with a third order parametric form. Consider an arbitrarily small displacement vector δx around x^*. To a second order, we can write

$$T(x^* + \delta x) = x^* + J_T(x^*)\delta x + \frac{1}{2}\delta x^T \mathbb{H}_T(x^*)\delta x, \tag{7}$$

where $J_T(x^*)$ and $\mathbb{H}_T(x^*)$ are the Jacobian matrix and Hessian tensor of the map $T(x)$ at the saddle point. The idea here is to determine a function $f(u)$ that determines the normal displacement of the manifold at position u along the tangent line l_u, touching the manifold at x^*. In this representation, the parametric form of the local manifold takes the vector form

$$\mathcal{W}_u^{loc}(x^*, u) = x^* + u\hat{u} + f(u)\hat{v}, \tag{8}$$

where $\hat{u}$ is the unit unstable eigenvector of $J_T(x^*)$, satisfying

$$J_T(x^*)\hat{u} = \lambda_u \hat{u}, \tag{9}$$

with $\lambda_u > 1$, and $\hat{v}$ is perpendicular to $\hat{u}$. Using Eq. (9), it can be shown that a vector of magnitude u aligned with the unstable direction $\hat{u}$ gets stretched by a factor $\lambda_u + \kappa u$, in the unstable direction, with the parameter κ given by

$$\kappa = \frac{1}{2}\sum_{i,j,k=1}^{2} u_i u_j u_k T_{i,jk}, \tag{10}$$

where u_i are the coordinates of $\hat{u}$ in some set of orthogonal coordinates, and $T_{i,jk} = \frac{\partial^2}{\partial x_j \partial x_k} T_i(x_1, x_2)\Big|_{x^*}$ are the map derivatives with respect to these coordinates.

If we represent the phase space points by their displacements (u, v) along $\hat{u}$ and $\hat{v}$ with respect to the fixed point p^*, it can be shown that the normal displacement function satisfies

$$T_v[u, f(u)] = f(\lambda_u u + \kappa u^2). \tag{11}$$

This comes because the effect of T over a point in the manifold is moving it by a factor $\lambda_u + \kappa u$ along the unstable direction and displacing it normally to a new distance given by $f(\lambda_u u + \kappa u^2)$. Provided that we are close to the saddle, we can use (7) in the new coordinates to write-down the LHS of (11), which leads to a consistency relation for f,

$$\begin{aligned} &uT_{v,u} + f(u)T_{v,v} + \tfrac{1}{2}[u^2 T_{v,uu} + 2uf(u)T_{v,uv} + f^2(u)T_{v,uv}] \\ &\quad = f(\lambda_u u + \kappa u^2). \end{aligned} \tag{12}$$

In practice, we can use a polynomial expansion for f,

$$f(u) = au^2 + bu^3 + \cdots, \tag{13}$$

where 1 and u are absent because of the chosen coordinates. Provided that (12) is valid for any small u, we have that the coefficients resulting from replacing $f(u)$ in (12) must vanish independently. This allows us to relate the coefficients of f with the local properties of the map, i.e.,

$$a = \frac{T_{v,uu}}{2(\lambda_u^2 - T_{v,v})}, \quad b = \frac{a(T_{v,uv} - 2\kappa\lambda_u)}{\lambda_u^3 - T_{v,v}}, \ldots. \tag{14}$$

In the Appendix, we provide additional information on how to obtain the Hessian elements in (14) for an arbitrary planar map in arbitrary coordinates. With this, we have the information required to write explicitly a parametric form of the manifold near the saddle point x^* and, consequently, we are able to determine, to a leading order, one primary segment of the manifold that we will call the *zeroth segment*,

$$P_0 : \{\mathcal{W}_u^{loc}(x^*, u),\ u_0 \le u < (\lambda_u + \kappa u_0)u_0\}, \tag{15}$$

for some $u_0 << 1$. Numerically speaking, a representation of the local manifold can be determined to machine precision by making the highest order term of the manifold expansion to be below the roundoff error. In practice, we can check the performance of the local approximation by applying the map repeatedly over an initial condition obtained by $\mathcal{W}_u^{loc}(x^*, u_0)$ for some small u_0. In Fig. 3, we compare the performance of a linear and cubic expansions of the local manifold for one saddle of the Henon map[25] with the classical parameters $a_H = 1.4$ and $b_H = 0.3$.

In regular situations, a linear approximation of the local manifold may be sufficient,[20] but having higher orders in the expansion of $f(t)$ have important advantages in practical applications, given that a larger primary segment can store more preimages required to obtain numerically the global manifold. For instance, the primary segment between the 4th

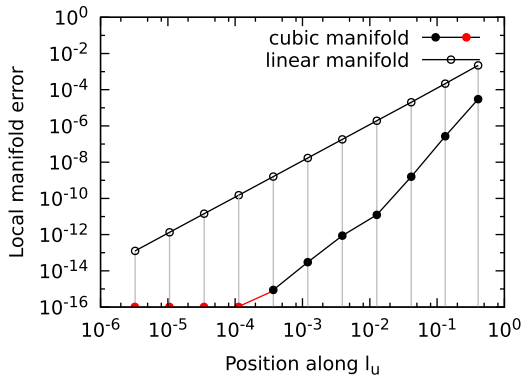

FIG. 3. Distance between the mapped points from $\mathcal{W}_u^{loc}(x^*, 10^{-6})$ and the local manifold for the simple linear approximation of the local manifold and an approximation with a cubic normal displacement function. For the first four iterates, the cubic manifold error is numerically zero (but here are illustrated at the minimum precision), and can be regarded as *exact*.

and 5th iterates of the cubic Henon manifold can generate preimages to machine precision along a portion of size 10^{-3}, while the linear manifold can only generate preimages with precision 10^{-13} between the initial condition and its first iterate, in a portion of size 10^{-6}. Clearly, there is an important gain when using higher order approximations of the manifold, in this example, a 1000-fold increase in available space with 1000-fold increase in precision (assuming machine precision around 10^{-16}).

Numerical indistinguishability between the actual manifold and its functional approximation guarantees that they will be equally affected by roundoff errors due to the application of the map itself, i.e., approximation errors will not propagate numerically if they were numerically nonexistent. In this context, general methods based on parametrization functions valid for high-dimensional systems can be used as well.[26] Generalizations for continuous systems are also available,[23] allowing us to approximate the manifold along the flow instead of in a cutting surface (the Poincaré section).[24]

IV. COMMENTS ON NON-REFINING ADVECTION ROUTINES

Provided that we identified an appropriate parametric form of the zeroth segment, the unstable manifold can then be written as the following semi-infinite union:

$$\mathcal{W}_u(x^*, T) = \widetilde{x^* x_\epsilon} \cup P_0 \cup P_1 \cup \cdots \cup P_i \cdots, \qquad (16)$$

where $P_{i+1} = T[P_i]$ and $\widetilde{x^* x}$ is the union of inverse mappings of P_0 which can be approximated by the parametric form $\mathcal{W}_u^{loc}(x^*, t)$ for $t \in (0, t_0)$.

With this simple definition, we can compute a finite representation of the invariant manifold to the desired extension, provided we know how to calculate $T[P_i]$ and we know one segment P_0. Formally speaking, if we know how to compute $T(y)$ for any $y \in P_i$, then we are able to compute $T[P_i]$, but mapping a set of uniformly distributed points in P_i will not, in general, lead to evenly distributed set of points in P_{i+1}.

As we do not know *a priori* which distribution of points in P_0 will lead to a uniform discretization of P_n, an interim solution consists in discretizing P_0 uniformly with a large number of nodes, although, eventually, the stretching and folding mechanism will overcome the excess points, and the segments will become poorly resolved.

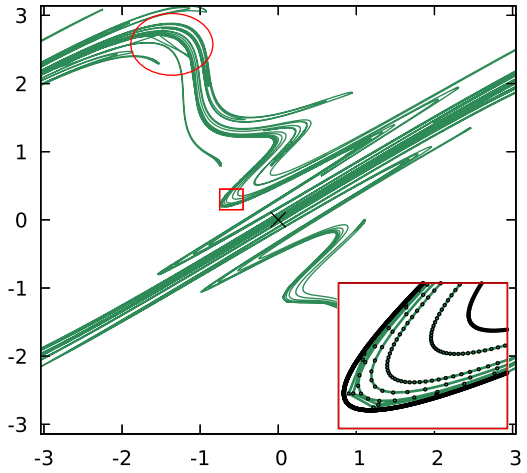

FIG. 4. Unstable manifold portion of the saddle $x^* = (0, 0)$ for the Chirikov-Taylor map with $k = 1.5$. The base segment P_0 was uniformly discretized with 4662 points, and the portion contains 25 primary segments. In the red circle, we can see a poorly resolved region, and the red inset shows the effect of stretching for different layers of a homoclinic lobe.

In Fig. 4, we show a short portion of the unstable manifold of the period-*one* saddle of the Chirikov-Taylor map,[27]

$$y_{n+1} = y_n + k \sin x_n, \qquad (17)$$

$$x_{n+1} = x_n + y_{n+1} \qquad (18)$$

for $k = 1.5$. Although the resulting curve appears smooth, close inspection shows the undesired effects of uniform discretization in P_0. The segment stretching leads to a complex mix of over-resolved and under-resolved portions of the manifold. In Sec. V, we introduce an adaptive method that allows us to determine the discretization of P_0 that leads to a well resolved discretization of an arbitrary P_n.

V. MAPPING-REFINEMENT METHOD

In this section, we introduce a refinement method for producing a suitable *exact* discretization of the manifold which satisfies some predefined resolution criteria by limiting the distance between subsequent nodes and the angles between consecutive secant lines. The word *exact* is used here to refer to the procedure by which nodes in an arbitrary segment are obtained from the *zeroth* segment, given that it can be determined to machine precision. More precisely, the only source of error in this case is the application of the mapping itself. For explicit mappings, it is the accumulated roundoff error, while for Poincaré maps, it is the inherent error of the numerical integration routine.

The *exact* method is then a procedure to obtain the most reliable discretization of the manifold for a prescribed finite precision, while the actual curve between each pair of nodes must be approximated by some suitable method.

Consider the following initial discretization of P_0:

$$P_0 \to \{x_{0,1}, x_{0,2}, \ldots, x_{0,M}\}, \qquad (19)$$

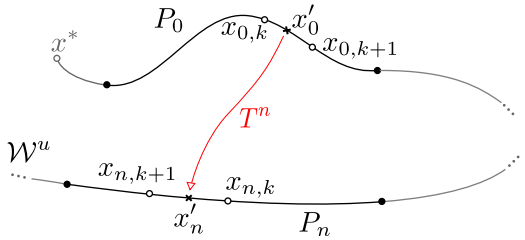

FIG. 5. The discretization of the nth segment may be improved by inserting new points at specific locations in the *zeroth* segment and applying T^n to populate the nth segment in a controlled fashion.

where the "$\rightarrow$" symbol is used instead of "$=$" to indicate that we are only *representing* the continuous set P_0 by a discrete set of points. The initial set of points can be obtained by evaluating

$$x_{0,i} = L_\epsilon\left(\frac{i-1}{M}\right) \tag{20}$$

for $i = 1, 2, \ldots, M$, M is a small number, usually < 10. Then, the induced discretization of the segment P_n is

$$P_n \rightarrow \{x_{n,1}, x_{n,2}, \ldots, x_{n,M}\}, \tag{21}$$

where

$$x_{n,i} = T^n(x_{0,i}). \tag{22}$$

As mentioned before, the resulting points of P_n will be unevenly spaced due to the non-uniform stretching of the primary segments, but this can be solved by adding new points to P_n at specific locations. For instance, if some resolution criterion is violated between $x_{n,k}$ and $x_{n,k+1}$, we need to insert a new manifold point x'_n between these points. Since we do not have a parametric representation for P_n, we need to obtain the new points from initial conditions in the first segment P_0, where we do have a parametric form given by (8). Then, we calculate x'_0 between $x_{0,k}$ and $x_{0,k+1}$ in P_0 and calculate $x'_n = T^n(x'_0)$, which is the required refinement point (Fig. 5). This procedure can be iterated until the discretization of P_n satisfies the desired resolution requirements.

The refinement procedure must result in evenly spaced points for low curvature regions and a higher density of points in high curvature regions. Such a scale-invariant resolution is desired if we require a reliable description of densely packed portions of the curve, or if we need to study the intersection between manifolds. In Fig. 6, we show the quantities involved in resolution conditions. In general, the length of the chord l_i connecting the nodes x_i and x_{i+1} is required to be below some small value l_c. This chord belongs to an infinite secant line that forms and angle θ_i with the secant line containing

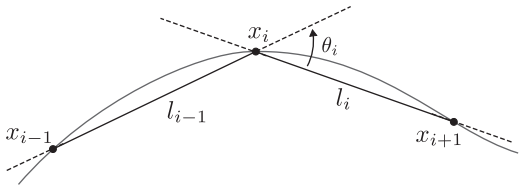

FIG. 6. Relevant quantities for the resolution criteria. The chord l_i connects the nodes x_i and x_{i+1}, and the angle θ_i is defined between the secant lines containing l_i and l_{i-1}.

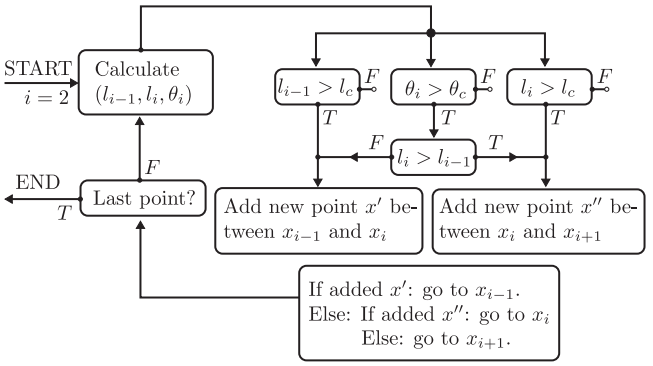

FIG. 7. Refinement procedure to produce a discretization of P_n satisfying the resolution criteria and preventing superfluous clustering. The points x' and/or x'' are obtained by applying T^n to corresponding points in P_0.

the chord l_{i-1}. Analogously, the inter-secant angle θ_i must be below some predefined value θ_c. Provided that l_c and θ_c are sufficiently small, the arcs connecting the points x_{i-1}, x_i, and x_{i+1} will not differ much from straight lines. With this, we establish that most of the geometric information is contained in the nodes instead of the arcs connecting them. Then, the small details contained in the parameters that determine the arcs are used to guarantee the manifold differentiability.

Upon violation of the resolution criteria, a refinement procedure must be carried out as illustrated in Fig. 7. In short, a new point is introduced between x_i and x_{i+1} if the chord l_i is larger that the critic distance l_c, or if l_i is the longest chord in an angle that exceeds some small critical value θ_c. This simple procedure and the rules of motion in Fig. 7 prevent clustering of new nodes and distribute the new entries evenly along the manifold. The procedure is iterated until the criteria are satisfied for all nodes in the segment P_n, then these nodes are mapped to obtain an initial discretization of P_{n+1} and so on.

This method differs from others in that we do not try to extrapolate the location of new nodes based on the information of previous nodes,[19,20] we start with an initial set of nodes generated by mapping the nodes of the previous segment, then perform the refinement operations following Fig. 7. A similar method is mentioned by Goodman and Wróbel,[21] but it adds two points instead of one and does not discuss on movement rules, which in our experience have important consequences for the efficiency and reliability of the refinement.

In Fig. 8, we show the same portion of Fig. 4 calculated with the mapping-refinement method. The calculation was done so that the number of nodes in P_0 is the same for the uniform discretization example, and the number of calls to the map function is the same for both calculations. In the inset region of Fig. 8, it is clear that the resulting nodes are evenly spaced in regions of low curvature and accumulate in the high curvature regions as required. Although the results from the mapping-refinement method have no error intrinsic to the manifold tracing, they have some inherent error sources, as the roundoff error when applying explicit maps or the error of numerical integration routine when using a Poincaré map.

Before introducing the interpolation-mapping approach, let us discuss a relevant limitation of the presented method. Since all the points in the manifold are seeded in P_0, the mapping-refinement method is numerically intensive; more

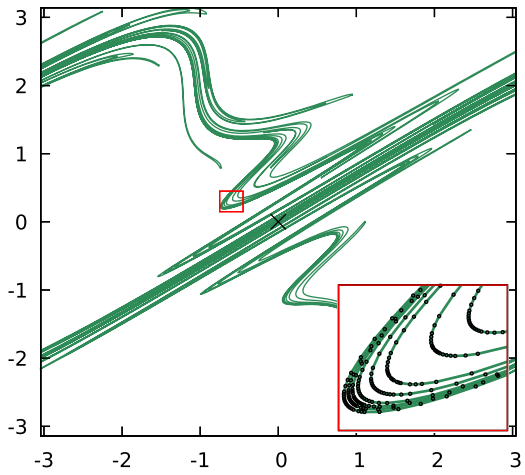

FIG. 8. Unstable manifold portion of the Chirikov-Taylor map saddle with $k = 1.5$. The adaptive generation of initial conditions on segment P_0 was used to satisfy $l_c = 0.1$, $\theta_c = 10^\circ$ for each of the 25 segments depicted.

precisely, if M_n is the number of points required to resolve the nth segment, the total number of calls to the map function when tracing n segments of a manifold is

$$Nc(n) = nM_n. \tag{23}$$

Assuming that the stretching mechanism leads on average to an exponential growth in the primary segments, we obtain

$$Nc(n) \propto ne^{\lambda n} \tag{24}$$

for an appropriate $\lambda > 0$. Consequently, the presented method can be computationally expensive for manifold calculations involving a large number of primary segments, although in most situations a few tens of segments are sufficient to obtain sufficient information on the manifold geometry. A more fundamental problem lies in the finite-precision of the numerical representation, which limits the number of different initial conditions that can be represented in P_0, and can be insufficient to resolve a given P_n due to the exponential growth of M_n. This is why it is important to use high order interpolants for the zeroth segment, as this allows us to work with a large primary segment. In practical situations, the stretching mechanism can be sufficiently large for two neighbor initial conditions in a linear representation of P_0 separated by the minimum representable numerical difference in coordinates to become separated after a few mappings by a distance that exceeds the resolution limit l_c in the phase space.

VI. INTERPOLANT-MAPPING METHOD

In Sec. V, we introduced a refinement method to produce a suitable discretization of the exact manifold to any desired resolution and extent. Despite our control over the calls to the map function and a precise definition of the refinement regions, the resulting procedure can be computationally intensive (but far less intensive than a non-refining procedure). To reduce the computational cost we can move to an approximation paradigm,[19] where the refinement of segment P_{n+1} is based on the approximation of initial conditions in segment P_n, instead of initial conditions in P_0.

In this section, we concentrate on producing an approximated continuous representation for P_{n+1} based on an approximated representation of P_n. This is formally closer to the original composition presented in (16), but, in practice, we use the refinement methods presented in Sec. V to define an iterative scheme that allows us to produce reliable interpolants from a previous segment in the manifold.

Assume that we have a planar parametric curve $\bar{P}_n(s) : \mathbb{R} \to \mathbb{R}^2$ for $s \in [s_l, s_r]$ that approximates the points in the nth segment P_n to a given precision ε. This is

$$\forall\, s \in [s_l, s_r], \quad \exists x \in P_n : |\bar{P}_n(s) - x| < \varepsilon. \tag{25}$$

In other words, the points in $\bar{P}_n(s)$ differ from those in P_n by at most a distance ε. To approximate the segment P_{n+1}, we can infer its behavior from an appropriate set of nodes

$$x_i = T[\bar{P}_n(s_i)]; \quad i = 0, 1, 2, \ldots, N, \tag{26}$$

where s_0 and s_N are the parameters corresponding to the endpoints of the segment P_{n+1}. The set $s_0, s_1, \ldots, s_N$ is chosen so that the curve between any pair $\{x_i, x_{i+1}\}$ cannot differ much from a straight line. The procedure to do this is analogous to that presented in Fig. 7, where a new node between x_i and x_{i+1} is added when the resolution criteria are not met. The new point is obtained by parametric bisection

$$x' = T\left[\bar{P}_n\left(\frac{s_i + s_{i+1}}{2}\right)\right]. \tag{27}$$

After determining an appropriate set of nodes for the whole domain of P_{n+1}, the interpolant curve to approximate it is a piecewise vector function

$$\bar{P}_{n+1}(s) = \begin{cases} f_0(\gamma_0, s), & s \in [s_0, s_1], \\ \vdots & \\ f_{N-1}(\gamma_{N-1}, s), & s \in [s_{N-1}, s_N], \end{cases} \tag{28}$$

where $f_i : \mathbb{R} \to \mathbb{R}^2$ and γ_i's are adjustable parameters that determine the local properties of the curve and can be determined by imposing geometrical constrains on the interpolant pieces f_i.

A. The interpolant model

Consider the following expression for the position vector along the interpolant of the ith arc:

$$\vec{f}_i(\gamma_i, s) = \vec{x}_i + t\vec{l}_i + h_i(\gamma_i, t)\hat{z} \times \vec{l}_i, \tag{29}$$

where $\vec{x}_i$ is the position vector of node x_i, $\vec{l}_i = \vec{x}_{i+1} - \vec{x}_i$, and $t \in [0, 1]$ is the normalized position along the chord line joining x_i and x_{i+1} (see Fig. 9). The function $h_i(\gamma_i, t) : \mathbb{R} \to \mathbb{R}$ is proportional to the normal distance between the interpolant curve $f_i(s)$ and the chord $\overline{x_i, x_{i+1}}$, and satisfies $h_i(0) = h_i(1) = 0$, which guarantees that the curve passes through the nodes x_i and x_{i+1}. Notice also that the L.H.S. in (29) depends on the global parameters s, and the R.H.S. depends on the normalized parameter t so that there is a function $s = g(t)$ that allows us to make the transformation from the local parameter t to the global one s. The interesting part of this arc representation is that the bare geometrical aspects of the curve are contained in the first half of the expression $\vec{x}_i + t\vec{l}_i$, and the fine tuning is carried by the *shape function*

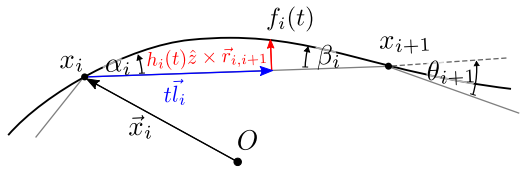

FIG. 9. The position along the model curve can be decomposed into three vectors. One defines the first node x_i, the second is the displacement along the chord joining two nodes, and the third gives the normal displacement of the arc with respect to the chord.

$h_i(\gamma_i, t)$, in the second part, which contains the error adjustable parameters γ_i. Notice also that a good choice of the partition nodes results in $h_i(\gamma_i, t) << 1$, everywhere in the interval, guaranteeing that the main geometry is well described by the nodes themselves and only small (but extremely important) details are described by $h_i(\gamma_i, t)$.

By definition, the arc representation (29) is continuous across the nodes x_i, but we also require the curve model to be differentiable everywhere. Since the interpolant is smooth inside the arcs, we concentrate on the nodes and require

$$\left.\frac{d\vec{f}}{ds}\right|_{s=s_i^-} = \left.\frac{d\vec{f}}{ds}\right|_{s=s_i^+} \tag{30}$$

for all s_i in the partitioning. In terms of the local representations of the interpolant, this becomes

$$\left.\frac{dt}{ds}\,\frac{d\vec{f}_{i-1}}{dt}\right|_{t=1} = \left.\frac{dt'}{ds}\,\frac{d\vec{f}_i}{dt'}\right|_{t'=0}, \tag{31}$$

where t and t' are the corresponding local parameters of the arcs $i-1$ and i. Because the global parameter s has the same meaning across the node, the differential ds is the same in both sides, and we are left with a simpler relation that does not depend on the global parameter

$$\left.\frac{d\vec{f}_{i-1}}{dt}\right|_{t=1} = \left.\frac{dt'}{dt}\,\frac{d\vec{f}_i}{dt'}\right|_{t'=0}. \tag{32}$$

The relation dt'/dt can be determined by the ratio of the projections of a line element $d\vec{r}$ along the secant lines $\overline{x_{i-1}x_i}$ and $\overline{x_ix_{i+1}}$, leading to

$$\frac{dt'}{dt} = \frac{l_{i-1}}{l_i}\frac{\cos\alpha_i}{\cos\beta_{i-1}}, \tag{33}$$

where α_i and β_{i-1} are the angles between the tangent line at x_i and the secant lines. In other words, α_i and β_i are the angles between the ith arc and its corresponding chord line at the end-points (see Fig. 9). Writing β_{i-1} as the difference between α_i and the inter-secant angle θ_i, we obtain a consistent equation for the differentiability at the node i,

$$\left.\frac{d\vec{f}_{i-1}}{dt}\right|_{t=1} = \left.\frac{l_{i-1}}{l_i}\frac{\cos\alpha_i}{\cos(\alpha_i-\theta_i)}\,\frac{d\vec{f}_i}{dt'}\right|_{t'=0}, \tag{34}$$

where the angles θ_i can be determined from the position of the nodes alone. For a suitable choice of the *shape function* $h_i(\gamma_i, t)$, the chord-tangent angles α_i determine the overall behavior of the model curve and can be considered as the fundamental parameters of our interpolant.

Using the explicit arc representation in (29) and the differentiability condition (34), we can relate the angles α_i with the derivatives of the shape function at the end-points

$$h_i'(0) = \tan\alpha_i \quad \text{and} \quad h_i'(1) = \tan(\alpha_{i+1} - \theta_{i+1}). \tag{35}$$

B. The simplest shape function

Requiring the shape function $h(\gamma_i, t)$ to be the lowest order polynomial, vanishing for $t = 0$ and $t = 1$, and allowing for different left and right derivatives, we obtain a cubic function as the simplest expression for the shape function

$$h_i(t) = a_i t(1-t)^2 - b_i t^2(1-t), \tag{36}$$

where $a_i = h_i'(0)$ and $b_i = h_i'(1)$ are the end-point derivatives, and b_i can in turn be related to the parameters of the next shape function using the conditions obtained from differentiability in (35)

$$b_i = \frac{a_{i+1} - m_{i+1}}{1 + a_{i+1}m_{i+1}}, \tag{37}$$

where $m_{i+1} = \tan\theta_{i+1}$. Given that the inter-chord angles θ_i are the resulting features of the discretization procedure, they are not adjustable parameters and are kept fixed. This leaves us with the set $\vec{a} = \{a_0, a_1, \ldots, a_N\}$ which can, in principle, be adjusted to obtain an interpolant $\bar{P}_{n+1}$ which is closest to the primary segment P_{n+1}. However, to adjust this set, an error functional must be minimized, and this requires obtaining more information about the curve being modeled. For instance, we can calculate a set of intermediate points $y_i = T[\bar{P}_n(s_i')]$ where $s_i' \in (s_i, s_{i+1})$ and minimize the functional

$$\varepsilon(\vec{a}) = \sum_{i=0}^{N-1} |\vec{f}_i(a_i, a_{i+1}) - \vec{y}_i| \tag{38}$$

by performing subsequent variations $\delta\vec{a}$ obtained from a Levenberg-Marquardt procedure.[28] As expected, this results in an interpolant that passes through every node and is closest to the intermediate points $\vec{y}_i$. However, there can be an arbitrary distance between the interpolant and the primary segment $\bar{P}_{n+1}$ in every other location without affecting the error functional. In fact it was observed that an appropriate guess of the set $\{a_0, a_1, \ldots, a_N\}$ performed better at arbitrary locations than the numerically optimized set, even when additional optimization constraints were applied, like requiring the interpolant arc-length to be small or limiting the domain of variation of the α_i's.

A suitable guess consists in requiring the tangent line on each node to bisect the inter-secant angle. In other words, $\alpha_i = \theta_i/2$, resulting in the following relations between parameters:

$$a_i = \frac{\sqrt{1+m_i^2} - 1}{m_i} \quad \text{and} \quad b_i = -a_{i+1} \tag{39}$$

with $m_i = \tan\theta_i$. This results in a very smooth curve passing through all the nodes, but as discussed before, the success of this approximation relies on leaving a minimum amount of information on the shape function. Most of the information must be contained in the node positions, and the interpolant between two nodes must differ very little from a straight line,

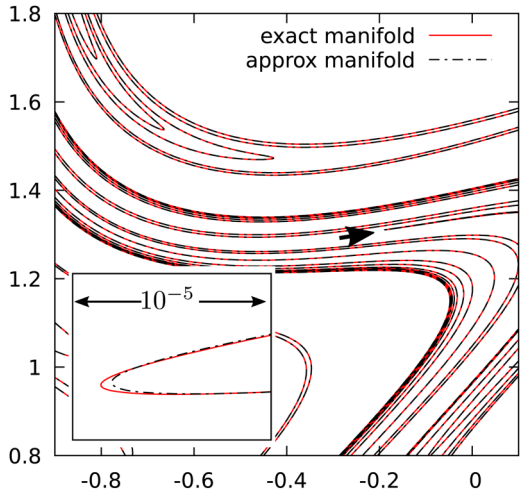

FIG. 10. Comparison between 26 primary segments of the exact and approximated unstable manifolds of the Chirikov-Taylor map for a region of phase space. To depict any difference between the manifolds we zoomed into an extreme corner, where differences below 10^{-6} develop.

i.e., the values of a_i must be very small. Notice that this is automatically satisfied for a good set of nodes because all inter-secant angles satisfy $\theta_i < \theta_c$ with $\theta_c << 1$.

We can estimate the maximum distance from the interpolant curve to the corresponding secant line in terms of the resolution parameters l_c and θ_c. Provided that $\theta_c << 1$, we have

$$H_c = l_c h_c \approx \frac{\theta_c l_c}{8}, \tag{40}$$

where θ_c is measured in radians and $h_c = h(1/2)$ for $a = b = \tan\theta_c$. This gives us a baseline to measure the interpolation error, which must be small in units of H_c.

C. Comparison to the *exact* calculation

In Fig. 10, we compare the approximated manifold and the *exact* one in a 1×1 region of the phase space for the Chirikov-Taylor map with $k = 1.5$. For this comparison, we traced 26 primary segments with $d_c = 0.01$ and $\theta_c = 3.0^\circ$ for both the exact and approximated calculation. This gives us a distance baseline of $H_c \approx 6.5 \times 10^{-5}$ so that the local interpolation error must satisfy $\varepsilon << H_c$. In the scale of Fig. 10, differences between the manifolds are not observable, and in fact they are not observable in any low or moderate-curvature region, because the distance between consecutive nodes of the manifold is much larger than the separation between the curves. To depict any difference we must look into very sharp corners, where any tiny amount of compression along the manifold amplifies the differences between the exact and approximated manifold.

To have a better perspective of the approximated manifold error, we can measure the distance between an exact node and its expected position from the manifold interpolant. This can be done by finding the normal projection of the exact node along the secant line between two nodes of the approximated manifold. This gives us the value of t in (29), and we can calculate the corresponding interpolant position.

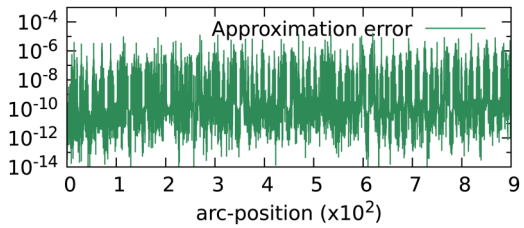

FIG. 11. Distance between the nodes of the exact manifold and their location from the manifold interpolant as a function of the arc-position along the manifold. The distance fluctuates widely but remains bounded below 10^{-5}.

In Fig. 11, we show the distance between the exact nodes and their corresponding estimation by the interpolants that compose the approximated manifold. Because the first segment of the approximated and exact methods is the same, we expect smaller errors for the first segments. However, the correlation between the nodes of the exact calculation and approximated method is quickly lost because of the difference in the construction methods, then the distance from the exact nodes to their estimated positions gives us a good estimate of the local error. An important feature of Fig. 11 is that the interpolant error does not grow along the manifold as a consequence of mapping approximated new nodes based on an interpolant curve. This indicates that the approximation method is stable, i.e., small errors introduced by the interpolation of new nodes get damped due to the compression perpendicular to the manifold.

For this example, the manifold error is quite small, as can be seen in Fig. 12, where the statistical distribution of distances of Fig. 11 is shown. The error of the interpolants that compound the approximated manifold concentrate around 10^{-9} and below 10^{-17}, and error values close to the baseline $H_{max} \approx 6.5 \times 10^{-5}$ show a very small probability. Remarkably, these results were obtained after setting the adjustable parameters $\{\alpha_0, \alpha_1, \ldots\}$ only by geometrical requirements. It is important to realize that errors below 10^{-17} must not be considered to be meaningful, since they are below machine precision, and their numerical representation is not reliable. However, it is important to keep them in the error histogram because they account for the events where the approximated and the *exact* manifolds were numerically identical.

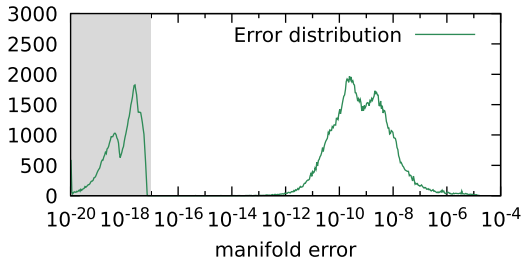

FIG. 12. Statistical distribution of the distances in Fig. 11. For a random position in the manifold there is a high probability of obtaining errors near 10^{-9}, and the probability of values near the baseline $\sim 10^{-5}$ is significantly small. The values in the shaded region below 10^{-17} are not numerically reliable because they fall below machine precision; however, we preserve them because their frequency indicates the number of events where the approximated and *exact* methods were numerically identical.

The resolution criteria led to 10^6 calls to the map function for the exact calculation and 10^5 calls for the approximated one. This factor *ten* reduction in the number of calculations is due to the seeding of a new initial condition in the segment previous to the segment under refinement, instead of the *zeroth* segment. The number of calculations involved in the approximated calculation can be approximated by

$$N_c^*(n) = \sum_{n'=0}^{n} M_{n'} \propto \sum_{n'=0}^{n} e^{\lambda n'}, \tag{41}$$

so that, for a large stretching rate λ and large number of primary segments n, the number of calls to the map approaches

$$N_c^*(n) \propto \frac{e^{\lambda n}}{1 - e^{-\lambda}}, \tag{42}$$

then, for a finite number of segments, the ratio to the number of calls for the exact calculations satisfies

$$\frac{N_c^*}{N_c} \lesssim \frac{\kappa}{n}, \tag{43}$$

where $\kappa = (1 - e^{-\lambda})^{-1} > 1$. This rapidly decreasing function of the number of segments n guarantees a sustained growth in efficiency as the number of primary segments increases.

VII. AN EXAMPLE APPLICATION

Now that we have illustrated the approximated manifold calculation for an explicit map, we consider a situation where the computational efficiency is more relevant, a continuous time dynamical system. Consider, for instance, the conservative Duffing oscillator with the Hamiltonian function

$$H(q,p,t) = p^2/4 - 2q^2 + q^4 + \epsilon q \cos(\omega t), \tag{44}$$

where q and p are conjugate variables and satisfy the Hamilton equations. Physically, q and p are the position and momentum of a particle in a double-well potential subjected to a periodic force field. In the unforced situation, particles with energy $E < 0$ are restricted to one side of the well, but in the forced situation, the external field enables the transition from one well to the other for energies moderately below *zero*. This problem has interest in modeling the increase of the transition rate over potential barriers induced by external monochromatic fields.[11] Moreover, the corresponding deterministic diffusion in the chaotic region competes with quantum-mechanical tunneling between wells.[29,30]

In the subject of magnetically confined plasmas this problem is equivalent to that of an asymmetric single-null tokamak discharge.[31] Here, small asymmetries cause some magnetic field lines to become chaotic around the plasma column and the external divertor coils, leading the charged particles to encounter the tokamak chamber.[4,5] The use of resonant magnetic perturbations to break the magnetic invariants in the separatrix region has important applications in the control of plasma edge instabilities and plays an important role in modern tokamak operation.

Broadly, the potential barrier penetration can be understood through the formation of a chaotic layer around the separatrix of the well, which overcomes the potential barrier of the integrable case, allowing chaotic orbits to wander in both sides of phase space. However, there are interesting situations where the transit between sides of the well is virtually suppressed for orbits in the chaotic layer during long extents of time, and manifold tracing provides relevant insight into the mechanisms involved in transport or lack of it.

In Fig. 13, we show 30 000 cycles of the stroboscopic position of the Duffing system for an arbitrary orbit in the chaotic layer with different forcing amplitudes. For $\epsilon = 0.025$, the orbit spends a long time on each side of the well with shorter interludes of global motion. As we increase the amplitude, the times spent in local motions become shorter, and global motion begins to dominate. For instance, at $\epsilon = 0.05$, periods of localized motion are very short compared to those of global motion.

To understand these transitions in a geometrical basis, we need to know which invariants control the motion in the chaotic region. From structural stability,[13] it is expected for the perturbed system to contain a saddle x_c^*, which is a time-dependent version of the unperturbed saddle at $(0,0)$. The invariant manifolds of this saddle are responsible for driving the chaotic orbits from one side of the well to the other, but this is not the only period-*one* saddle in the chaotic region. For $\omega = 1.5$, there are two resonant tori near the separatrix of the double well, one for each side of the well. For $\epsilon = 0.025$, they are destroyed by the perturbation creating period-*one* K.A.M. islands surrounded by a thin chaotic layer driven by the invariant manifolds of a helical saddle x_h^*. The chaotic layers of the central saddle and the islands are in contact, but their interaction depends on the perturbation strength.

In Fig. 14, we show a single orbit in the merged chaotic layers and an inset depicting the central and right period-*one* saddles with some of their invariant manifolds. The periodic orbits x_c^* and x_h^* were determined to 14 significant digits using a modified Levenberg-Marquardt algorithm.[28] For $\epsilon = 0.025$, a finite tracing of the invariants shows no entanglement between the manifolds of the central and the helical saddle. The lobes of the stable and unstable manifolds of x_h^* develop around x_h^* so that chaotic orbits near the helical saddle tend to remain so, leading to a slow diffusion from the chaotic

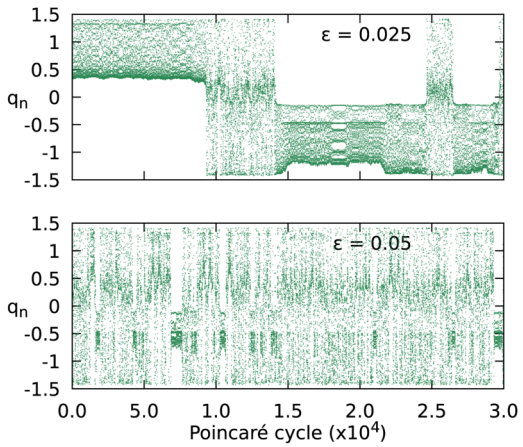

FIG. 13. The particle's position from the stroboscopic map of the Duffing system with $\omega = 1.5$ and two different amplitudes. Larger amplitudes lead to a predominantly global motion, while small ones cause spontaneous transitions between the different localized and global motions.

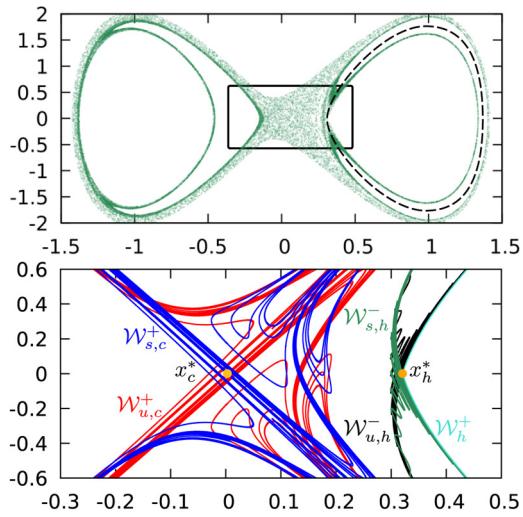

FIG. 14. For $\omega = 1.5$ and $\epsilon = 0.025$, the orbit transits between sides of the potential well spending long times near the helical saddles of period-*one* K.A.M. islands. The resonant torus is sketched with a dashed line. The inset shows finite portions of the invariant manifolds of the central saddle x^*_c and helical one x^*_h, exhibiting homoclinic intersections.

layer around the island to the global layer responsible for transitions, as if they were only weakly connected.

When the forcing amplitude is increased, the lobes of the stable and unstable manifolds of x^*_h develop around x^*_c, and vice versa, causing a heteroclinic connection between these saddles and a strong entanglement between their manifolds which results in a full mixing of the chaotic layers (Fig. 15). This transition from homoclinic to heteroclinic connection explains the transition from the alternating localized chaotic motion to the global chaotic dynamics, and leads to the suppression of the local motion features of around the period-*one* islands. Provided that there are transitions for the $\epsilon = 0.025$ case, there must be some heteroclinic connection between the saddles, and such can be observed after a rather

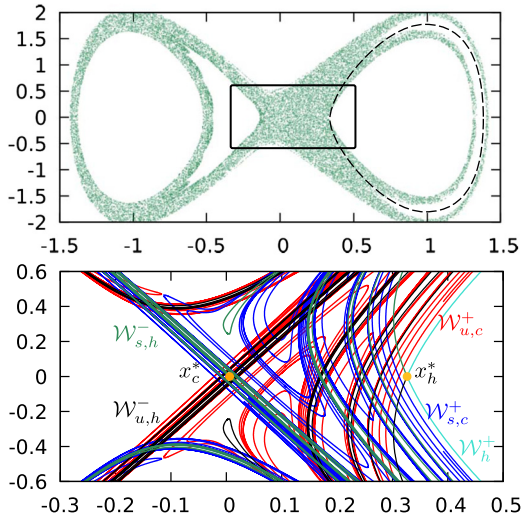

FIG. 15. For $\omega = 1.5$ and $\epsilon = 0.05$, the orbit wanders the chaotic region uniformly. The inset containing the central and helical saddles shows the development of heteroclinic connections between them, and a rather complex pattern of manifold intersections, so that diffusion in the chaotic region becomes more uniform.

extensive manifold tracing; however, this is a second-order feature and the homoclinic connections determine the most relevant features of the weak forcing situation.

VIII. CONCLUSIONS

In this paper, we introduced a mapping-refinement approach to discretize the exact invariant manifolds of planar maps. This intensive method prevents redundant calculations and makes the best use of every new orbit resulting in a lower computational cost when compared to non-refining approaches. An intensive non-refinement technique with the same computational cost results in a non-smooth representation of the manifold with under-resolved and over-resolved portions.

Then, we introduced an interpolant-mapping approach to approximate the invariant manifolds. Our interpolation method was based on the curve decomposition in bare and fine details, where the fine details were contained in a normal displacement function or *shape function*. This curve decomposition is new to our knowledge and does not involve any parametric optimization stage, which eases the method implementation.

With the approximation method, the efficiency was greatly increased with a small precision penalty due to the interpolation of the primary segments for seeding new orbits. Comparison between the exact and approximated manifold resulted in errors well below the determined baseline, even when the shape functions of the interpolant curve were chosen to be the simplest polynomial function with independent endpoint derivatives. This leaves space for further improvement if more elaborate shape functions are used, or even parametric optimization techniques, with the cautions mentioned in Sec. VI B.

To illustrate the different manifold tracing routines, we obtained the invariants for the Chirikov-Taylor map during the methods comparison, and used the approximation technique to study the chaotic transitions between local and global motions in the conservative Duffing oscillator, where the transition from homoclinic to heteroclinic connections between the central and helical saddles in the chaotic layer was evidenced in agreement with the observed intermittent dynamics.

ACKNOWLEDGMENTS

This work was developed with financial support from the National Council for Scientific and Technological Development (CNPq, Brazil) Grant No. 433671/2016-5, the São Paulo Research Foundation (FAPESP, Brazil) Grant Nos. 2012/18073-1 and 2011/19296-1, and the U.S. Department of Energy under DE-FC02-04ER54698 and DE-SC0012706.

APPENDIX: DETERMINATION OF HESSIAN ELEMENTS OF T

In Sec. III, we described with some detail how to determine the normal displacement function coefficients for an approximated local manifold near a saddle point of an arbitrary map. Any planar map $T : \mathbb{R}^2 \to \mathbb{R}^2$ consists of two

functions $T_{1,2}$, one for each dimension

$$T(x_1, x_2) : \begin{pmatrix} T_1(x_1, x_2) \\ T_2(x_2, x_2) \end{pmatrix}. \tag{A1}$$

The unstable unit vector $\hat{u}$ satisfies

$$\begin{pmatrix} T_{1,1} & T_{1,2} \\ T_{2,1} & T_{2,2} \end{pmatrix} \hat{u} = \lambda_u \hat{u} \tag{A2}$$

with $T_{i,j} = \frac{\partial}{\partial x_j} T_i(x_1, x_2)\Big|_{x^*}$, and its determination is elementary in two dimensions. The entries of $\hat{u}$ are related to the angle θ, between $\hat{u}$ and $\hat{x}_1$, by

$$\hat{u} = (\cos\theta, \sin\theta)^T = (c, s)^T. \tag{A3}$$

Coordinates (u, v) are such that u is the displacement along the unstable subspace with respect to the saddle x^*, and v is the displacement perpendicular to u. These coordinates are just a rotation by $-\theta$ of coordinates (x_1, x_2) and, analogously, the representation (T_u, T_v) of map T can be obtained by

$$\begin{pmatrix} T_u(u, v) \\ T_v(u, v) \end{pmatrix} = \begin{pmatrix} c & s \\ -s & c \end{pmatrix} \begin{pmatrix} T_1(x_1, x_2) \\ T_2(x_2, x_2) \end{pmatrix}. \tag{A4}$$

Using elementary transformation rules, we can obtain the required elements for the calculations in (14). For the Jacobian elements, we have

$$T_{v,u} = -csT_{1,1} - s^2 T_{1,2} + c^2 T_{2,1} + csT_{2,2}, \tag{A5}$$

$$T_{v,v} = s^2 T_{1,1} - csT_{1,2} - csT_{2,1} + c^2 T_{2,2}, \tag{A6}$$

and for the Hessian elements

$$\begin{aligned} T_{v,uv} = {} & cs^2 T_{1,11} - s(c^2 - s^2) T_{1,12} - cs^2 T_{1,22} \\ & - c^2 sT_{2,11} + c(c^2 - s^2) T_{2,12} + c^2 sT_{2,22}, \end{aligned} \tag{A7}$$

$$\begin{aligned} T_{v,uu} = {} & -c^2 sT_{1,11} - 2cs^2 T_{1,12} - s^3 T_{1,22} \\ & + c^3 T_{2,11} + 2c^2 sT_{2,12} + cs^2 T_{2,22}, \end{aligned} \tag{A8}$$

where $T_{i,jk} = \frac{\partial^2}{\partial x_j \partial x_k} T_i(x_1, x_2)\Big|_{x^*}$ can be obtained by elementary differentiation of the original map or can be obtained numerically by finite differences when an explicit form is not available.

[1] A. M. Ozorio de Almeida, *Hamiltonian Systems: Chaos and Quantization* (Cambridge University Press, 1988).
[2] A. J. Lichtemberg and M. A. Liberman, *Regular and Chaotic Dynamics* (Springer, 1992).
[3] J. D. Meiss, "Symplectic maps, variational principles, and transport," Rev. Mod. Phys. **64**, 795 (1992).
[4] E. da Silva, I. Caldas, R. Viana, and M. Sanjuán, "Escape patterns, magnetic footprints, and homoclinic tangles due to ergodic magnetic limiters," Phys. Plasmas **9**, 4917 (2002).
[5] T. Evans, R. Moyer, and P. Monat, "Modeling of stochastic magnetic flux loss from the edge of a poloidally diverted tokamak," Phys. Plasmas **9**, 4597 (2002).
[6] P. J. Morrison, "Magnetic field lines, Hamiltonian dynamics, and nontwist systems," Phys. Plasmas **7**, 2279 (2000).
[7] A. Wingen, M. Jakubowski, K. H. Spatschek, S. S. Abdullaev, K. H. Finken, and M. Lehnen, "Traces of stable and unstable manifolds in heat flux patterns," Phys. Plasmas **14**, 042502 (2007).
[8] A. Wingen, O. Schmitz, T. E. Evans, and K. H. Spatschek, "Heat flux modeling using ion drift effects in DIII-D H-mode plasmas with resonant magnetic perturbations," Phys. Plasmas **21**, 012509 (2014).
[9] T. E. Evans, R. K. W. Roeder, J. A. Carter, B. I. Rapoport, M. E. Fenstermacher, and C. J. Lasnier, "Experimental signatures of homoclinic tangles in poloidally diverted tokamaks," J. Phys. Conf. Ser. **7**, 174 (2005).
[10] D. Ciro, T. Evans, and I. Caldas, "Modeling non-stationary, non-axisymmetric heat patterns in DIII-D tokamak," Nucl. Fusion **57**, 016017 (2017).
[11] L. E. Reichl and W. M. Zheng, "Field-induced barrier penetration in the quartic potential," Phys. Rev. A **29**, 2186 (1984).
[12] J. Aguirre, R. L. Viana, and M. A. F. Sanjuán, "Fractal structures in nonlinear dynamics," Rev. Mod. Phys. **81**, 333 (2009).
[13] J. Guckenheimer and P. Holmes, *Nonlinear Oscillations, Dynamical Systems and Bifurcations of Vector Fields* (Springer-Verlag, 1983).
[14] T. Kroetz, M. Roberto, E. C. da Silva, I. L. Caldas, and R. L. Viana, "Escape patterns of chaotic magnetic field lines in a tokamak with reversed magnetic shear and an ergodic limiter," Phys. Plasmas **15**, 092310 (2008).
[15] H. Kants and P. Grassberger, "Repellers, semi-attractors, and long-lived chaotic transients," Physica D **17**, 85 (1985).
[16] H. E. Nusse and J. A. Yorke, "A procedure for finding numerical trajectories on chaotic saddles," Physica D **36**, 137 (1989).
[17] P. Moresco and S. P. Dawson, "The pim-simplex method: An extension of the PIM-triple method to saddles with an arbitrary number of expanding directions," Physica D **126**, 36 (1999).
[18] D. Sweet, E. Nusse, and J. A. Yorke, "Stagger-and-step method: Detecting and computing chaotic saddles in higher dimensions," Phys. Rev. Lett. **86**, 2261 (2001).
[19] D. Hobson, "An efficient method for computing invariant manifolds of plannar maps," J. Comput. Phys. **104**, 14 (1993).
[20] B. Krauskopf and H. Osinga, "Growing 1D and quasi-2D unstable manifolds of maps," J. Comput. Phys. **146**, 404 (1998).
[21] R. Goodman and J. Wróbel, "High-order bisection method for computing invariant manifolds of two-dimensional maps," Int. J. Bifurcation Chaos **21**, 2017 (2011).
[22] B. Krauskopf, H. Osinga, E. J. Doedel, M. E. Henderson, J. Guckenheimer, A. Vladimirsky, M. Dellnitz, and O. Junge, "A survey of methods for computing (un)stable manifolds of vector fields," Int. J. Bifurcation Chaos **15**, 763 (2005).
[23] M. Breden, J. Lessard, and J. D. M. James, "Computation of maximal local (un)stable manifold patches by the parameterization method," Indagat. Math. New Ser. **27**, 340 (2016).
[24] X. Cabré, E. Fontich, and R. de la Llave, "The parameterization method for invariant manifolds III: Overview and applications," J. Differ. Equ. **2018**, 444 (2005).
[25] H. Hénon, "A two-dimensional mapping with a strange attractor," Commun. Math. Phys. **50**, 69 (1976).
[26] M. Fumming and T. Küpper, "Numerical calculation of invariant manifolds for maps," Numer. Linear Algebra **1**, 141 (1994).
[27] B. V. Chirikov, "A universal instability of many-dimensional oscillator systems," Phys. Rep. **52**, 263 (1979).
[28] D. W. Marquardt, "An algorithm for least-squares estimation of nonlinear parameters," SIAM J. Appl. Math. **11**, 431 (1963).
[29] T. Dittrich, F. Grossmann, P. Hänggi, B. Oelschlägel, and R. Utermann, "Coherent and incoherent dynamics in a periodically driven bistable system," in *Stochasticity and Quantum Chaos—Proceedings of the 3rd Max Born Symposium* (1995), Vol. 317, p. 39.
[30] M. J. Davis and E. J. Heller, J. Chem. Phys. **75**, 246 (1981).
[31] P. C. Stangeby, *The Plasma Boundary of Magnetic Fusion Devices* (IOP Publishing, 2000).